frontiers in Energy Research

ORIGINAL RESEARCH
published: 11 December 2020
doi: 10.3389/fenrg.2020.609417

Atomic Layer Deposition of SnO_2-Based Composite Anodes for Thin-Film Lithium-Ion Batteries

*Bo Zhao, Arpan Dhara, Jolien Dendooven and Christophe Detavernier**

Department of Solid State Sciences, COCOON Research Group, Ghent University, Ghent, Belgium

Transition metal oxides are promising anode materials for lithium-ion batteries thanks to their good electrochemical reversibility, high theoretical capacities, high abundance, and low cost. The mechanism of lithium insertion or deintercalation into or from these metal oxides can be different depending upon their lattice structure or chemical nature. Synergistic effects obtained from mixing different metal oxides with (dis)similar lithiation/delithiation mechanisms (intercalation, conversion and alloying) can significantly improve the device performances. In this research, we systematically investigate the impact on electrochemical properties of SnO_2 thin-films upon mixing with TiO_2, Fe_2O_3 and ZnO. In these pure thin-films, SnO_2 displays conversion- as well as alloying-type lithiation and serves as the host material, whereas TiO_2 represents an intercalation-type anode material, Fe_2O_3 exhibits conversion reactions and ZnO expresses alloying during lithiation-delithiation processes. Importantly, all the composite thin-films have an intermixed structure at the atomic scale, as they are precisely prepared by the atomic layer deposition method. The electrochemical properties demonstrate that the composite thin-films show better performance, either higher capacities or better cycling retentions, than the individual constituent material (SnO_2, TiO_2, Fe_2O_3 or ZnO). Overall cycling stability improves to a great extent along with a slight increase in capacity with the addition of TiO_2. The supplement of Fe_2O_3 in the SnO_2–Fe_2O_3 composite thin-films moderately improves both capacity and retention, while the SnO_2–ZnO composite electrodes demonstrate a good cyclability and stabilize at a relatively high capacity. The systematic investigation of synergistic effects on the different types (intercalation, conversion and alloying) of metal oxide composites is expected to provide guidance towards the development of composite anode materials for lithium-ion batteries.

Keywords: atomic layer deposition, synergistic effect, intercalation, conversion, alloying, thin-film, SnO_2, lithium-ion battery

OPEN ACCESS

Edited by:
Xiangbo Meng,
University of Arkansas, United States

Reviewed by:
Aidong Li,
Nanjing University, China
Xifei Li,
Xi'an University of Technology, China

****Correspondence:***
Christophe Detavernier
christophe.detavernier@ugent.be

Specialty section:
This article was submitted to Electrochemical Energy Conversion and Storage, a section of the journal Frontiers in Energy Research

Received: *23 September 2020*
Accepted: *16 November 2020*
Published: *11 December 2020*

Citation:
Zhao B, Dhara A, Dendooven J and Detavernier C (2020) Atomic Layer Deposition of SnO_2-Based Composite Anodes for Thin-Film Lithium-Ion Batteries. Front. Energy Res. 8:609417. doi: 10.3389/fenrg.2020.609417

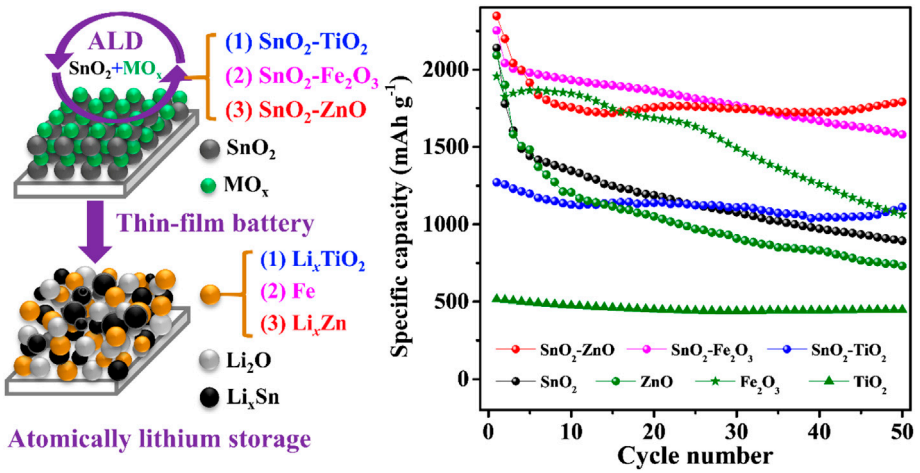

GRAPHICAL ABSTRACT | ALD of atomically intermixed SnO_2-TiO_2, SnO_2-Fe_2O_3 and SnO_2-ZnO composite thin-film electrodes to reveal the electrochemical synergistic effects on different types of metal oxide as anode materials for Li-ion batteries.

INTRODUCTION

Among different electrochemical energy storages devices, lithium-ion batteries (LIBs) are popular and widely used due to their unique virtues, such as low self-discharge rate, long cycle life, high conversion efficiency, and easy to manufacture flexible designs etc. With the growing needs for high power/energy density applications such as electric vehicles, grid storages etc., new demands for LIBs are requiring. However, traditional electrodes like graphite (anode, theoretical capacity is 372 mAh g^{-1}) and $LiCoO_2$ (cathode, theoretical capacity is 274 mAh g^{-1}) are unable to satisfy anymore. Therefore, it is crucial to find new materials which can fulfill these new demands (Chen et al., 2018a; Kim et al., 2019; Pender et al., 2020).

Anode materials for LIBs can be typically divided into the categories of carbonaceous material (e.g., graphite, graphene and carbon nanotubes), silicon and metal oxides (Su et al., 2014; Qi et al., 2017; Fang et al., 2019; Roselin et al., 2019). Among others, transition metal oxides have received tremendous interests due to their high theoretical capacities, good redox reversibility and ease of synthesis (Reddy et al., 2013; Zheng et al., 2018; Fang et al., 2020). There are three mechanisms of lithium storage in transition metal oxides: intercalation, conversion and alloying. For intercalation-type anodes, the lithium ions can be reversibly inserted/removed into/from the host material without chemical deformation and slight volume deterioration. As an example, (lithium-) titanium dioxide, is a typical representative of intercalation-type materials. With the limited lithium uptake per volume and high molar mass, the intercalation-type anodes are more suitable for applications which require longer stability (Zhu et al., 2012; Yan et al., 2015; Yuan et al., 2017). For the alloying-type, metal oxide firstly irreversibly converts to metal and then reacts with lithium to form lithium-metal alloys during the charging process, the following discharging process is the reversible dealloying steps of lithium-metal to metal. Sn- and Ge-based oxides are typical belonging to the alloying-type anode (Wei et al., 2013). The lithium-metal alloying and dealloying process provides the advantage of high lithium storage capability which is certainly good for the high capacity, but the accompanying severe volume change during charge-discharge is the fatal shortcoming (Zhang, 2011; Liu et al., 2017). This issue can be solved to some extent for the conversion-type metal oxides. The formed metals during the charging process do not alloy and dealloy with lithium anymore, instead, accompanying the reduction and oxidation. The metallic nanonetwork embedded in a Li_2O matrix formed after the reaction can improve the overall conductivity of the electrode (Wadewitz et al., 2013; Bruck et al., 2016; Lu et al., 2018). This essential merit can effectively elucidate the pulverization problem caused by volume changes and allow capacity improvement owing to their multiple redox reaction. However, the overall improvement in capacity and stability is limited to a certain extent. A summary of typical materials corresponding to the three types of anodes, and their advantages and drawbacks are listed in **Table 1**.

Even though the three types of metal oxide have their advantages, their shortcomings of either low capacity or tremendous volume changes together with the poor electronic conductivity make it hard to undertake the task of a good battery material individually. A strategy to effectively combat the bad impacts is using two different phases while react towards lithium at two different electrochemical potentials (vs. Li/Li^+) in one composite electrode. Regarding this aspect, the hybrid AO_x-BO_y (A, B are different metal) electrodes are expected to sequentially alleviate the volume expansion and provide a highway for charge transfer in the two phases, guiding to a high reversible capacity and rate performance compared with pure phases. There are literatures reporting a synergistic effect of two different metal oxides leading to a significant improvement in cyclability and capacity (Wu et al., 2015; Zhao et al., 2016). SnO_2 is a well-studied material and it exhibits a typical conversion and following alloying reaction mechanism towards lithium (Chen and Lou, 2013; Zhao et al., 2015b; Zoller et al., 2019). There are many

TABLE 1 | Intercalation, alloying and conversion-type of anodes and their advantages and drawbacks.

Reaction type	Samples	Advantages	Drawbacks
Intercalation	Carbonaceous material (Lithium-)titanium oxide	Safety, low cost Safety, low cost, long cycle life, high power capability, trivial volume changes	High potential hysteresis, high irreversible capacity Low capacity, low power density
Alloying	Si, Ge, Sn, Sb etc. and -based oxide, phosphide, sulfide, nitride	Environmentally friendly, widespread, low cost, high theoretical capacity, high energy density	Huge volume changes, irreversible capacity, huge capacity fading
Conversion	Fe, Mn, Co, Ni, etc. and -based oxide, phosphide, sulfide, nitride	Environmentally friendly, widespread, low cost, high theoretical capacity, appropriate operating potential	Low Coulombic efficiency, poor capacity retention, unstable SEI

researches on the synergistic effect between SnO_2 and another metal oxide, like SnO_2–CuO (Cheong et al., 2018), SnO_2–TiO_2 (Yi et al., 2016), SnO_2–Fe_2O_3 (Kint et al., 2019), SnO_2–ZnO (Zhao et al., 2019), SnO_2–Co_3O_4 (Zhao et al., 2015a) and SnO_2–In_2O_3 (Kim et al., 2007) etc. as composite anode material for LIBs.

In this report, SnO_2–TiO_2, SnO_2–Fe_2O_3, and SnO_2–ZnO composite thin-films intermixed at the atomic scale were precisely prepared by the atomic layer deposition (ALD), and were used as model electrodes to systematically investigate their evolved electrochemical properties. Here ALD provides the advantages of precise thickness and composition control of the thin-film electrodes, which in turn allows for the investigation of the transport process of lithium ions through the active material without the interference of polymeric binder and carbon black as used in conventional composite electrodes (Ha et al., 2012). Thin-film electrodes react with lithium fast and effectively which encourage the cyclic voltammetry curve with higher resolution and thus can be used to analyze more details of the peak and furtherly deconvolute overlapping reactions (Ferraresi et al., 2018).

Three typical representative substances which exhibit a different reaction mechanism as pure thin-films (intercalation-type TiO_2, conversion-type Fe_2O_3 and alloying-type ZnO) have been mixed with SnO_2 material. The precisely controlled compositions were verified by X-ray photoemission spectroscopy (XPS), surface morphologies measured with atomic force microscopy (AFM), synergistic effect mechanisms were mainly investigated by cyclic voltammetry (CV), electrochemical impedance spectroscopy (EIS), cycling stability and rate capability.

EXPERIMENTAL

The thin-film samples were prepared in a home-built high vacuum ALD system (base pressure is below 5×10^{-6} mbar) (Xie et al., 2007; Musschoot et al., 2009; Dendooven et al., 2010). Tetrakis(dimethylamino)tin(IV) (TDMASn, 99.9%, Sigma Aldrich) and H_2O was used to deposit SnO_2, where TDMASn bubbler heated to 45°C, and the corresponding conveyer tube to the chamber held at 50°C (Zhao et al., 2019). To deposit TiO_2 and ZnO, tetrakis(dimethylamido)titanium (TDMAT, 99.99%, Sigma Aldrich) and diethyl zinc (DEZn, 95%, Strem Chemicals) were chosen as metal sources respectively, and H_2O used as the co-reactant. TDMAT, DEZn and H_2O were kept at room temperature and all the conveyer tubes were kept at 50°C (Deng et al., 2015). Tert-butyl ferrocene (TBF, 98%, Strem Chemicals) and oxygen plasma was used to deposit Fe_2O_3 (Ramachandran et al., 2014). The TBF bubbler was kept at 75°C, and the conveyer tube to the chamber was heated to 85°C. The parameters for generating oxygen plasma are as follows: the input oxygen pressure is 1×10^{-2} mbar, a radio frequency remote plasma source at a frequency of 13.56 MHz and the output power is 200 W. The substrate temperature was held at 150°C for all the depositions. The ALD of SnO_2–MO_x composites were conducted by using the supercycles based sequence of $n \times (x\ SnO_2 + y\ MO_x)$ (M = Ti, Fe or Zn), where x is the cycle number of

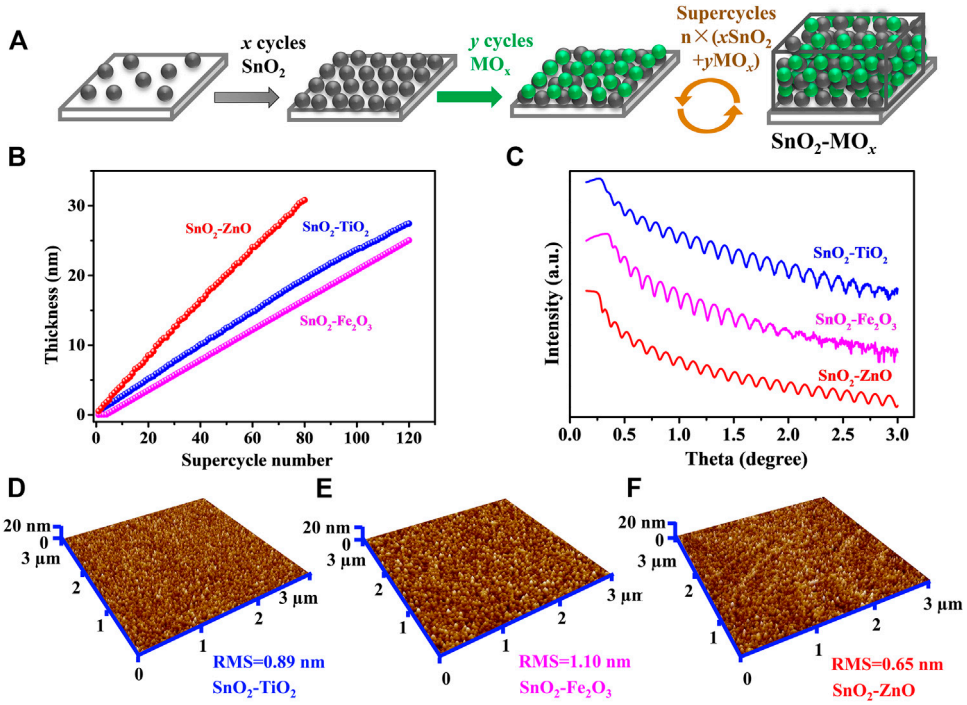

FIGURE 1 | ALD of SnO_2–MO_x composite thin-films. **(A)** Scheme of the supercycles approach $n \times (x\ SnO_2 + y\ MO_x)$. **(B)** Thickness as a function of supercycle number from *in-situ* SE and **(C)** XRR curves. Three-dimensional view AFM images of the ALD **(D)** SnO_2–TiO_2, **(E)** SnO_2–Fe_2O_3 and **(F)** SnO_2–ZnO thin-films. The scale is 3 × 3 µm.

ALD SnO_2, y is the cycle number of ALD MO_x, and n represents the supercycle repetition number. The value of x and y was chosen to achieve atomic scale intermixing rather than multilayer deposition, as illustrated in **Figure 1A**.

Thin-films were deposited on Si (100) substrates for growth characterizations. *In-situ* spectroscopic ellipsometry (SE) was used to monitor the thickness of the thin-film in between ALD cycles using a Woollam M-2000 spectrometer fitted directly onto the ALD reactor. X-ray reflectometry (XRR) was used to measure the thickness and density of the as-deposited thin-films, in which XRR was performed on a Bruker D8 diffractometer with Cu Kα (λ = 0.154 nm) radiation. Surface morphologies and roughness were characterized by atomic force microscopy (AFM, Bruker Dimension Edge system) in tapping mode and scanning electron microscopy (SEM, Quanta 200 F FEI). X-ray photoelectron spectroscopy (XPS) measurements were performed using a Thermo Scientific™ with Al Kα (λ = 0.834 nm) X-rays generated at 15 kV and 70 W. C 1 s assigned at 284.6 eV was used to calibrate the binding energy.

Electrochemical characterizations were conducted in an argon-filled glovebox (H_2O < 1 ppm, O_2 < 1 ppm) with a home-built potentiostat/galvanostat (Dobbelaere et al., 2017) connected to a three-electrode set (**Figure 3A**). The thin-films deposited on the Si-20 nm SiO_2-40 nm TiN substrates were used as the electrodes for electrochemical tests. Lithium ribbon (99.9%, Sigma-Aldrich) was used as counter and reference electrode, and 1 M $LiClO_4$ in propylene carbonate (PC, 99%, io-li-tec) was used as Li^+ electrolyte. The CV was measured at a scan rate of 1 mV s^{-1} from 0.1–3.0 V (vs. Li/Li^+). The EIS was conducted at the frequency from 100 KHz to 10 mHz $m = \rho \times V = \rho \times s \times t$ was used to calculate the mass (m) of active materials, where the contact area (s) is 1.05 cm^2, while the density (ρ) and the thickness (t) were obtained from XRR results.

RESULTS AND DISCUSSIONS

Atomic Layer Deposition Growth and Characterizations of Thin-Films

Three thin-film materials were prepared, i.e., SnO_2 intermixed with TiO_2, Fe_2O_3 and ZnO respectively, at a ratio of 1:1, labeled as SnO_2–TiO_2, SnO_2–Fe_2O_3, and SnO_2–ZnO. The ALD process sequence was 120 × (SnO_2 + 2TiO_2) for SnO_2–TiO_2, 120 × (SnO_2 + 4Fe_2O_3) for SnO_2–Fe_2O_3, and 80 × (2SnO_2 + 3ZnO) for SnO_2–ZnO. **Figure 1B** displays the thickness as a function of supercycle number from *in-situ* SE, and the results show that the thickness is 27.3, 25.6 and 31.1 nm for 120 cycles of SnO_2–TiO_2, 120 cycles of SnO_2–Fe_2O_3 and 80 cycles of SnO_2-ZnO, respectively. **Figure 1C** shows the recorded XRR curves of the three thin-films where no fundamental differences can be found in the thickness profile. All samples exhibit clear Kiessig fringes, which is indicating a smooth surface. The simulation results indicate thicknesses of 28, 25 and 30 nm which are in line with the *in-situ* SE result, roughness of 0.62, 0.97 and 0.51 nm, and densities of 5.2, 5.6 and 5.9 g cm^{-3} for the SnO_2–TiO_2,

TABLE 2 | The thickness, density, roughness and XPS composition of SnO_2–TiO_2, SnO_2–Fe_2O_3, and SnO_2–ZnO composite thin-films by ALD.

Sample	ALD deposition	Thickness (nm)		Density (g cm^{-3})	Roughness (nm)		XPS composition (at %)		
		In-situ SE	XRR		XRR	AFM	Sn	M	O
SnO_2–TiO_2	120 × (SnO_2 + 2TiO_2)	27.3	28	5.2	0.62	0.89	22	26	52
SnO_2–Fe_2O_3	120 × (SnO_2 + 4Fe_2O_3)	25.6	25	5.6	0.97	1.10	15	31	54
SnO_2–ZnO	80 × (2SnO_2 + 3ZnO)	31.1	30	5.9	0.51	0.65	21	22	57

SnO_2–Fe_2O_3 and SnO_2–ZnO thin-films respectively. The surface morphologies were obtained from AFM in tapping mode. The corresponding three-dimensional surface morphologies of the as-deposited composite thin-films are shown in **Figures 1D**–F. The surface topography of all three thin-films were found to be smooth, homogeneous with uniform grains. The root mean square (RMS) roughness values are 0.89, 1.10 and 0.65 nm obtained for SnO_2–TiO_2, SnO_2–Fe_2O_3 and SnO_2–ZnO thin-film, respectively, which are well in agreement with the XRR results. **Table 2** summarizes the thickness, density, and roughness values obtained from the *in-situ* SE and XRR data fittings.

The XRD patterns of the composite thin-films and binary oxide reference thin-films are shown in **Figure 2A**. All the patterns clearly reveal (although with the existence of Si background) the amorphous structure except for the ZnO reference film which shows diffractions of (002) and (101) indicating a polycrystalline wurtzite structure (PDF card No. 01-074-9940). In order to evaluate the chemical composition and gain insight into the chemical bonding environment of the composite thin-films, XPS was employed. The full survey spectra presented in **Figure 2B** show the peaks of Sn, Ti, Fe, Zn and O elements, while no other impurities are observed. The calculated atomic concentration values indicate a nearly 1:1 atomic ratio between SnO_2 and MO_x in the SnO_2–MO_x composite thin-films, as shown in **Table 2**. From the XPS depth profiles in **Figure 2C**, the Ti content in SnO_2–TiO_2, Fe content in SnO_2–Fe_2O_3 and Zn content in SnO_2–ZnO are almost unchanged throughout the respective thin-film, indicating there is no bilayer or laminate structure and uniform mixing between SnO_2 and MO_x has been achieved. The binding energy of the Ti $2p_{1/2}$ and Ti $2p_{3/2}$ peaks for SnO_2–TiO_2 are centered at 465.5 and 459.7 eV, as displayed in **Figure 2D**, where the splitting between Ti $2p_{1/2}$ and Ti $2p_{3/2}$ was 5.8 eV indicating the presence of Ti^{4+} (Li et al., 2015a). In **Figure 2E**, Fe $2p_{3/2}$ and Fe $2p_{1/2}$ are centered at 710.3 and 723.5 eV demonstrating the trivalent state of iron present in SnO_2–Fe_2O_3 thin-films (Gu et al., 2017). **Figure 2F** shows peaks aligned at 1020.8 and 1043.9 eV which corresponding to the Zn $2p_{3/2}$ and Zn $2p_{1/2}$ of Zn^{2+} (Zhao et al., 2019). Based on the above results, it can be summarized that 25–30 nm thick, uniform, smooth and atomically intermixed SnO_2–TiO_2, SnO_2–Fe_2O_3 and SnO_2–ZnO composite thin-films were grown successfully with an atomic ratio of SnO_2/MO_x at ~1:1.

Electrochemical Characterization of SnO_2

To evaluate the synergistic effect between SnO_2 and MO_x, the electrochemical studies of a pure SnO_2 thin-film was performed as a reference. **Figure 3B** shows the initial three cycle CV curves where five distinct cathodic peaks can be observed during lithiation and three anodic peaks during delithiation. In the early stage of lithiation from 1.5 to 0.8 V, multiple reactions lead to the formation of intermediate Li_2SnO_3 and metallic Sn phases (corresponding to **Eqs 1** and **2**). Further lithiation to the range between 0.6 and 0.4 V results in another intermediate Li_8SnO_6 and metallic Sn phases (**Eqs 3** and **4**). At the potential of ~0.25 V, the accumulated metallic Sn alloyed to Li_xSn phases (**Eq. 5**). Above 1.5 V, Sn is partially re-oxidized to SnO_x, and then repeats in the following cycle. Two intermediate phases, Li_2SnO_3 and Li_8SnO_6, were detected during lithiation of the thin-film SnO_2 electrode. These results match very well with the reported SnO_2 thin-film model electrodes (Ferraresi et al., 2018).

It is worth mentioning that the reaction mechanisms of SnO_2 with Li^+ usually differ between the thin-film based electrodes and the slurry-based conventional electrodes. This is mainly because of the existence of conductive additives and binders in the latter (Wen et al., 2007; He et al., 2013; Jahel et al., 2014; Xie et al., 2015). Conventional SnO_2 slurry electrodes exhibit two obvious cathodic peaks around 0.87 and 1.18 V, attributed to the Li_2O formation and electrolyte decomposition, and other redox peaks appear at 0.15 and 0.56 V are linked to the multistep Li_xSn formation. The multistep conversion and alloying mechanism of the SnO_2 thin-film electrode makes it obtain a theoretical capacity of 1,491 mAh g^{-1}, in which 711 mAh g^{-1} comes from the irreversible conversion reaction and 783 mAh g^{-1} from the reversible alloying step. The evolution of SnO_2 thin-films during lithiation can be summarized as follows (Kim et al., 2014; Ferraresi et al., 2018):

$$2SnO_2 + 2Li^+ + 2e^- \rightarrow SnO + Li_2SnO_3 \quad (1)$$

$$SnO + 0.67Li^+ + 0.67e^- \rightarrow 0.67Sn + 0.33Li_2SnO_3 \quad (2)$$

$$1.33Li_2SnO_3 + 2.67Li^+ + 2.67e^- \rightarrow 0.67Sn + 0.67Li_8SnO_6 \quad (3)$$

$$0.67Li_8SnO_6 + 2.67Li^+ + 2.67e^- \rightarrow 0.67Sn + 4Li_2O \quad (4)$$

$$Sn + xLi^+ + xe^- \leftrightarrow Li_xSn \quad (5)$$

Synergistic Effect Between SnO_2 and TiO_2

To unveil the influence of TiO_2 anode material, which belongs to intercalation-type in its bulk form, intermixed into the SnO_2 matrix on the lithiation/delithiation process, the electrochemical performance of SnO_2–TiO_2 composite thin-films were investigated. **Figure 4A** shows the CV curves of a pure TiO_2 reference thin-film in the initial three cycles where redox pair peaks assigned at 1.6 and 2.2 V corresponding to the Li^+ insertion and extraction into or from TiO_2 (**Eq. 6**). The overlap of the CV curves show the excellent $Ti^{+4}/Ti^{+(4-x)}$ reversibility during the charge-discharge process (Ban et al., 2013).

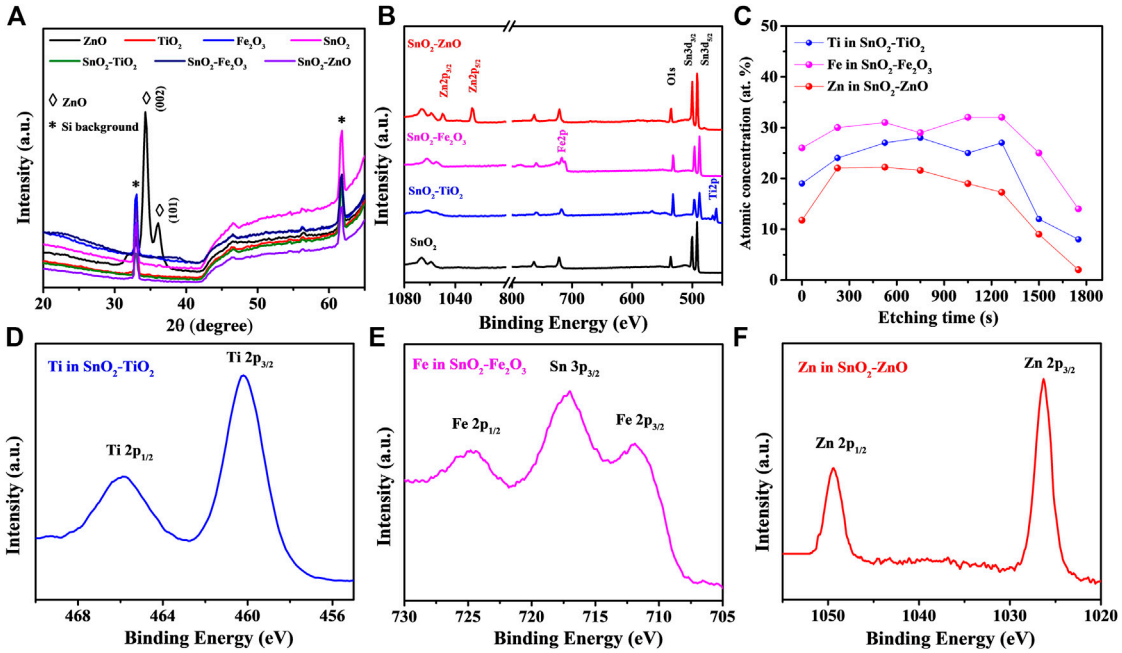

FIGURE 2 | (A) XRD patterns of SnO_2–MO_x composite and MO_x reference. XPS spectra of SnO_2–MO_x: **(B)** survey scans, **(C)** atomic concentration (at%) depth profiles and high-resolution scan of **(D)** Ti 2p in SnO_2–TiO_2, **(E)** Fe 2p in SnO_2–Fe_2O_3 and **(F)** Zn 2p in SnO_2–ZnO.

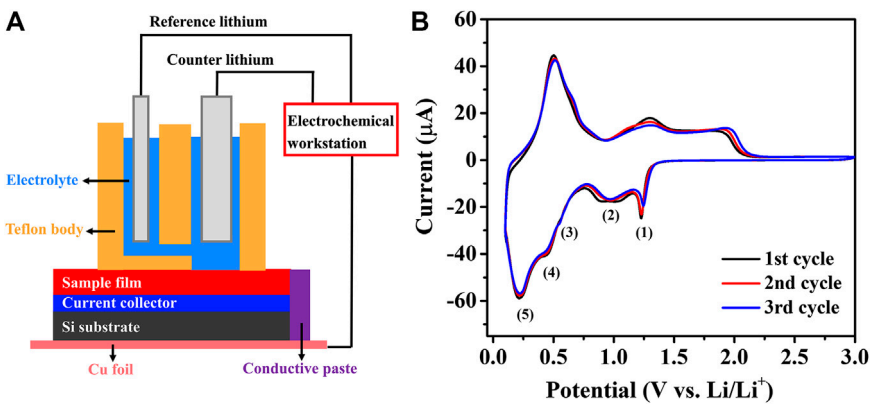

FIGURE 3 | (A) The configuration of battery evaluation setup used in this research. **(B)** Initial three cycle CV curves of ALD SnO_2 thin-film electrode.

$$xLi^+ + TiO_2 \leftrightarrow Li_xTiO_2 \quad (6)$$

Figure 4B displays the CV curves of the SnO_2–TiO_2 composite thin-film electrodes. In the first cathodic sweep, the first sharp peak around 1.6 V can be assigned to the lithium insertion into TiO_2. The huge peak around 0.9 V is probably related to the reductive transformation of SnO_2 to Sn/SnO (corresponding to **Eqs 1–3**). At very low potential, the peak located at 0.2 V is believed due to the formation of Li_xSn alloys (**Eq. 5**). During the anodic process, the broad peaks centered around 0.6 and 1.7 V correspond to the multi-step dealloying reactions from Li_xSn to Sn followed by oxidation of Sn to SnO_x, respectively. Furthermore, the anodic peak at 2.45 V is most likely linked to the Li^+ extraction from Li_xTiO_2. Notably, both sharp cathodic peaks around 0.9 and 1.6 V disappeared from the second cycle and a new broad peak appeared at around 1.3 V instead. The broad peak possibly resulted from the combination of Li_xTiO_2 and Li_ySnO_2 formation. Those differences between SnO_2 and SnO_2–TiO_2 suggest the obvious influence of TiO_2 intermixing with SnO_2, which would certainly affect the cycling performance. As expected, in **Figure 4C** the SnO_2 reference electrode displayed an initial capacity as high as 2,260 mAh g^{-1}, but it continuously and rapidly declined to 879 mAh g^{-1} after 50 cycles. On the other hand, the TiO_2 reference thin-film electrode delivered an initial capacity of 516 and 468 mAh g^{-1} after 50 cycles, exhibiting a capacity retention of 90.7%, which reflects the advantages of its cycling stability due to the insertion/extraction reaction mechanism. For the SnO_2–TiO_2

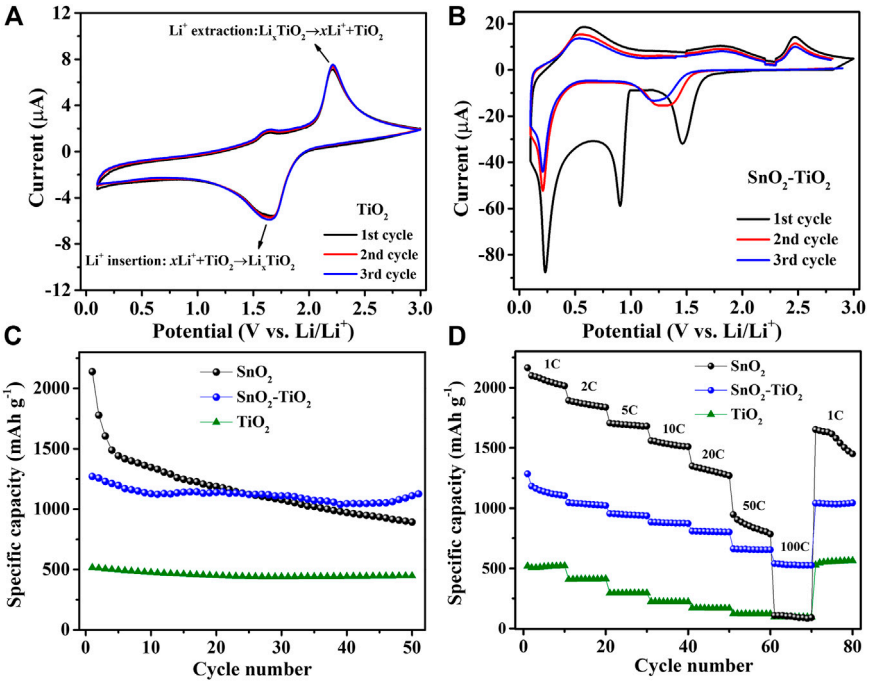

FIGURE 4 | CV curves of **(A)** TiO_2 and **(B)** SnO_2–TiO_2 composite electrodes. The comparison of SnO_2, TiO_2 and SnO_2–TiO_2 composite electrode: **(C)** cycling performance at 1C and **(D)** rate performance from 1 to 100 C.

composite electrode, the first discharge capacity is 1,270 mAh g^{-1}, followed by capacity fading during the initial cycles, yielding a capacity of 1,177 mAh g^{-1} that remained stable until the 50th cycle almost without any decay. In addition, in terms of rate performance (**Figure 4D**), as expected, the SnO_2 electrode showed worst capacity retention followed by SnO_2–TiO_2 and TiO_2. There is an obvious synergistic effect between SnO_2 and TiO_2, as the incorporation of TiO_2 avoids the dramatic capacity fading observed for the SnO_2 reference, while the presence of SnO_2 in the intermixed layer enhanced the capacity with respect to the TiO_2 reference (Chen et al., 2018b).

Synergistic Effect Between SnO_2 and Fe_2O_3

In the next attempt, we investigated the effects of atomically intermixing conversion-type Fe_2O_3 into a SnO_2 matrix. The CV curves of a pure Fe_2O_3 reference thin-film electrode are presented in **Figure 5A**. During the first lithiation process, three cathodic peaks are observed at 1.62, 0.98 and 0.76 V, respectively, corresponding to the following three lithiation steps (Wang et al., 2017):

$$x\mathrm{Li}^+ + \mathrm{Fe_2O_3} + x\mathrm{e}^- \rightarrow \mathrm{Li}_x\mathrm{Fe_2O_3} \quad (7)$$

$$(2-x)\mathrm{Li}^+ + \mathrm{Li}_x\mathrm{Fe_2O_3} + (2-x)\mathrm{e}^- \rightarrow \mathrm{Li_2Fe_2O_3} \quad (8)$$

$$4\mathrm{Li}^+ + \mathrm{Li_2Fe_2O_3} + 4\mathrm{e}^- \rightarrow 3\mathrm{Li_2O} + 2\mathrm{Fe} \quad (9)$$

At the initial stage of lithiation at 1.62 V, a small amount of lithium can react with Fe_2O_3 to form $Li_xFe_2O_3$ (**Eq. 7**). With further lithiation to 0.98 V, $Li_xFe_2O_3$ transformed to $Li_2Fe_2O_3$ (**Eq. 8**). At around 0.76 V, the sharp and intense peak corresponds to the complete conversion to metallic Fe (**Eq. 9**). In the anodic polarization process, several broad overlapping peaks are observed corresponding to the progressing oxidation of metallic Fe to Fe^{2+} and further to Fe^{3+}. **Figure 5B** shows the CV behavior of the SnO_2–Fe_2O_3 composite thin-film electrode, which is closely analogous to a combination of the CV behaviors of pure Fe_2O_3 (**Figure 5A**) and pure SnO_2 (**Figure 3B**). In the first cycle, there are three reduction peaks at 1.15, 0.93 and 0.31 V, and three oxidation peaks at 0.46, 1.05, and 1.97 V, respectively. The rather weak reaction peak at 1.15 V is assigned to the refoundation of $Li_xFe_2O_3$ and further reaction to $Li_2Fe_2O_3$ (**Eqs 7** and **8**). The sharp reduction peak around 0.93 V is attributed to the coinciding reduction reactions of SnO_2 to Sn/SnO and Fe^{2+} to Fe, and the formation of Li_2O. The peak at 0.31 V ascribes to the formation of a series of Li_xSn alloys. The delithiation reactions can be described by the following: the oxidation peaks at 0.46 and 1.05 V during the initial charge process can be attributed to the multi-step conversion of the Li_xSn alloy to Sn, the oxidation peak at 1.97 V can be attributed to the oxidation of Fe to Fe^{3+} (Li et al., 2015b). From the cycling performance, we can see that the SnO_2–Fe_2O_3 composite thin-film electrode achieves a discharge capacity of 1,580 mAh g^{-1}, while pure Fe_2O_3 shows a discharge capacity of 1,062 mAh g^{-1} after 50 cycles at 1 C (**Figure 5C**). The composite electrode holds 70.2% of the initial capacity after 50 cycles outperforming both the pure SnO_2 (38.9%) and Fe_2O_3 (54.3%) electrode. **Figure 5D** shows the further investigations of rate capabilities of all three electrodes. Among all, the pure Fe_2O_3 has the worst rate capability, while for the SnO_2–Fe_2O_3 composite electrode, although the specific capacity gradually decreases with the increase in current density, the capacity is always maintained higher than both SnO_2 and Fe_2O_3 at every delivered rate from 1 to

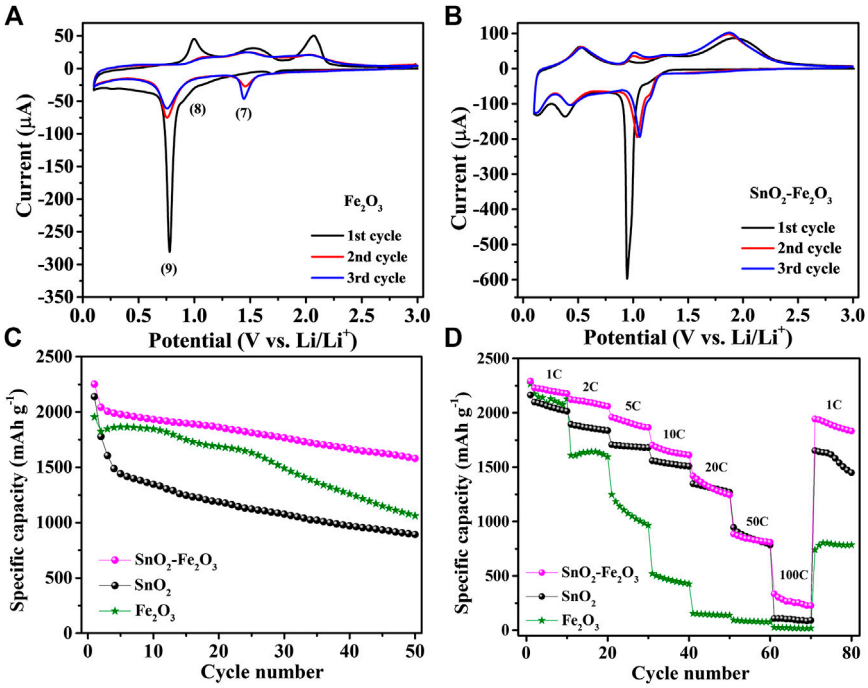

FIGURE 5 | CV curves of **(A)** conversion-type Fe_2O_3 and **(B)** SnO_2–Fe_2O_3 composite electrodes. The comparison of SnO_2, Fe_2O_3 and SnO_2–Fe_2O_3 electrode: **(C)** cycling performance at 1 C and **(D)** rate performance from 1 to 100 C.

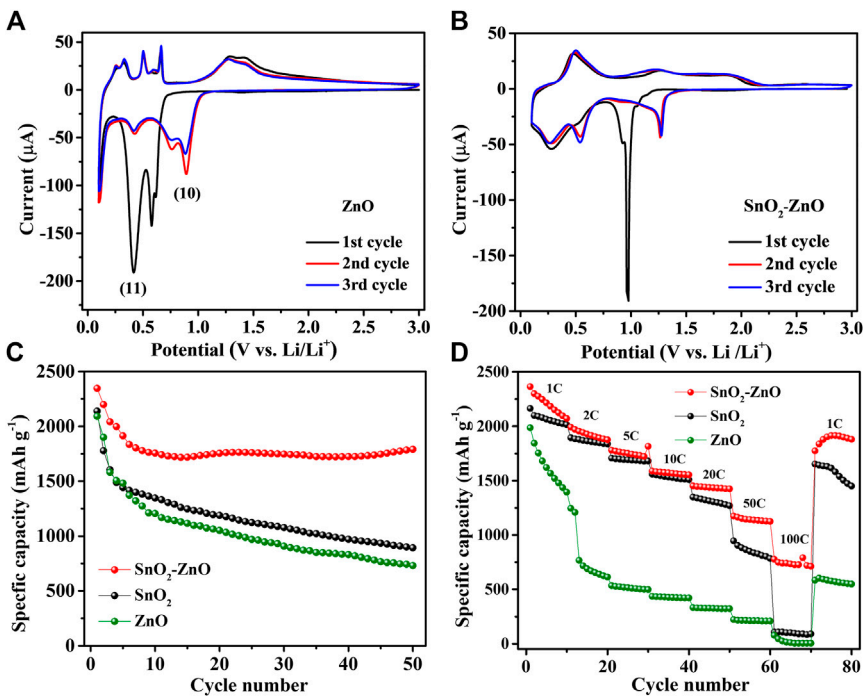

FIGURE 6 | CV curves of **(A)** alloying-type ZnO and **(B)** SnO_2–ZnO composite electrodes. The comparison of SnO_2, ZnO and SnO_2–ZnO composite electrode: **(C)** cycling performance at 1 C and **(D)** rate performance from 1 to 100 C.

TABLE 3 | The theoretical, initial charge-discharge capacity, Coulombic efficiency, the discharge capacity after 50 cycles at 1°C and the retention rate of all the investigated thin-film electrodes.

Material	Theoretical (mAh g^{-1})	Initial discharge (mAh g^{-1})	Initial charge (mAh g^{-1})	Initial Coulombic efficiency (%)	Discharge after 50 cycles (mAh g^{-1})	Retention (%)
SnO_2	1,491	2,260	1,908	84.4	879	38.9
TiO_2	336	516	488	94.6	468	90.7
Fe_2O_3	1,007	1,956	1,723	88.1	1,062	54.3
ZnO	978	2,092	1,808	86.4	730	34.9
SnO_2–TiO_2	626.2	1,270	1,177	92.7	1,126	88.7
SnO_2–Fe_2O_3	896.8	2,252	2,016	89.5	1,580	70.2
SnO_2–ZnO	849.3	2,386	2,169	90.9	1,795	75.2

100 C, especially significantly superior to Fe_2O_3. The obtained capacity from the SnO_2–Fe_2O_3 composite electrode is significantly higher than that of the pure SnO_2 or Fe_2O_3 reference electrode.

Synergistic Effect Between SnO_2 and ZnO

ZnO is known for exhibiting an alloying-type reaction mechanism towards lithium. Hence, ZnO-incorporated SnO_2 composite thin-films were prepared subsequently to explore the synergistic effect of two atomically intermixed anode materials with similar alloying-based mechanism. **Figure 6A** shows CV curves of pure ZnO thin-film electrode. The peak at 0.6 V in the first cathodic sweep aligned to the reduction of ZnO to Zn (**Eq. 10**), and the peaks at 0.4 and 0.12 V correspond to the multi-phase formation of Li_xZn alloys (**Eq. 11**). In the anodic sweep, several small peaks at 0.3, 0.47 and 0.61 V can be linked to the multi-dealloying steps from Li_xZn to Zn, the peak at 1.4 V is most probably due to the re-oxidation of Zn (Lu et al., 2017; Zhao et al., 2019).

$$2Li^+ + ZnO + 2e^- \rightarrow Zn + Li_2O \quad (10)$$

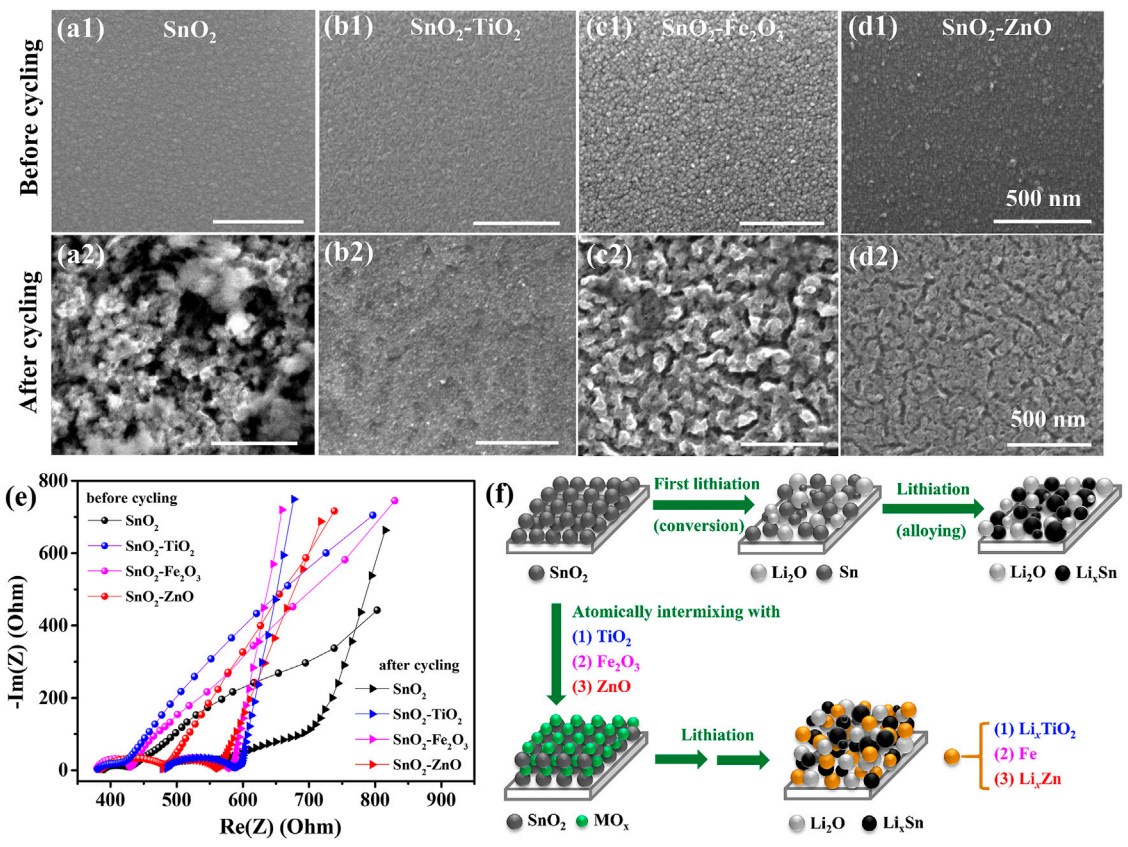

FIGURE 7 | SEM images of the morphology before and after cycling for the **(A1,A2)** SnO_2, **(B1,B2)** SnO_2–TiO_2, **(C1,C2)** SnO_2–Fe_2O_3 and **(D1,D2)** SnO_2–ZnO electrode. **(E)** EIS of the electrodes before and after cycling. **(F)** Schematic illustration of SnO_2 and the effect of atomically intermixing SnO_2 with MO_x on the lithiation mechanism.

$$xLi^+ + Zn + xe^- \rightarrow Li_xZn \quad (11)$$

The CV curves of the SnO_2–ZnO composite thin-film electrode are shown in **Figure 6B**. During the first cathodic scan, a sharp reduction peak around 0.98 V is observed which could be explained as the combination of the reduction of SnO_2 and ZnO to Sn and Zn, respectively. The peaks at 0.55 and 0.22 V probably correspond to the formations of Li_xSn and Li_xZn, respectively. During the first anodic scan, a peak at 0.54 V and a broad peak around 1.12 V are clearly distinguishable which could be attributed to multi-step dealloying reactions. The other two peaks at higher voltages (1.30 and ~2 V) are probably due to stepwise re-oxidation from Sn to SnO_x and Zn to ZnO. As observed in the cycling performance in **Figure 6C**, both the pure ZnO and SnO_2 thin-film electrodes suffer from significant capacity decay. However, the SnO_2–ZnO composite anode delivers a reversible capacity of 1,795 mAh g^{-1} after 50 cycles and exhibits 75.2% capacity retention with respect to the first cycle, which is much superior than that of 38.9% and 34.9% obtained from pure SnO_2 and ZnO respectively. The SnO_2–ZnO composite electrodes also exhibit an impressive rate capability. **Figure 6D** shows the rate capability behavior over 80 cycles from 1 to 100 C. The discharge capacities reach to 2,325, 1,992, 1,847, 1,642, 1,504, 1,209, and 743 mAh g^{-1} at 1, 2, 5, 10, 20, 50, and 100 C, respectively. Even after cycling at high rate of 100 C the capacity could return to 2,089 mAh g^{-1} when the current density returned back to 1 C. The SnO_2–ZnO composite electrodes offer a higher capacity than that of pure SnO_2 and Fe_2O_3 at every rate condition. Apparently, composite thin-film electrodes not only improve the capacity but also help in achieving improved cycling stability and rate performance.

Discussion on the Lithium Storage Mechanism

Table 3 lists a comparison of the details of capacities, Coulombic efficiencies and retention rates of all the investigated thin-film electrodes (pure references and composites). The charge capacity achieved in all the cases are higher than the theoretical capacity, which is due to the extremely thin films of active materials achieved by ALD (Mattelaer et al., 2015; Kint et al., 2019; Zhao et al., 2019; Li et al., 2020). The composite thin-films (SnO_2–TiO_2, SnO_2–Fe_2O_3 and SnO_2–ZnO) show better electrochemical properties, either higher capacity or better retention rate than their individual counter parts (SnO_2 and TiO_2, Fe_2O_3 or ZnO). With the addition of TiO_2, although the SnO_2 obtained smaller capacity, a significant improvement in cycling stability is observed in SnO_2–TiO_2 composite thin-film electrode. As for the SnO_2–Fe_2O_3 composite thin-film electrode, both the capacity and stability are moderately improved. In the case of SnO_2–ZnO composite thin-film electrode, notably, after few initial cycles of dropping, the capacity stabilizes and after 50 cycles it eventually offers the highest capacity among all the electrodes.

Figures 7A–D shows the surface morphology of SnO_2, SnO_2–TiO_2, SnO_2–Fe_2O_3 and SnO_2–ZnO electrode before and after cycling (after 50 charging-discharging cycles at 1 C). Before cycling, the as-prepared films are uniform and smooth with low roughness (as confirmed by AFM in Figures1D–F). After cycling, all the investigated films became much rougher, but in general, the morphology changes of the composite electrodes are less than that of pure SnO_2 reference. The SnO_2 electrode surface with large amounts of needle-like dendrites formed a porous structure after cycling which demonstrated the distortion by the lithiation and delithiation process. The SnO_2–TiO_2 surface kept relative smooth compared with others, indicating that there are mild volume changes when charged/discharged. While for the SnO_2–Fe_2O_3 and SnO_2–ZnO composite electrode, many islands surrounded by cracks are formed on the surface. The situation for SnO_2–Fe_2O_3 is worse than for SnO_2–ZnO. EIS before and after cycling was also conducted to gain further insight into the composite electrodes. As shown in **Figure 7E**, by comparing the size of the arcs, the diameters of the semicircles greatly increased after cycling, indicating an increase of the charge-transfer resistance. SnO_2–TiO_2, SnO_2–Fe_2O_3 and SnO_2–ZnO composite electrodes increased less than pure SnO_2, suggesting that the composite electrodes improved the electronic conductivity and among the composites SnO_2–ZnO is the most remarkable. Based on the results of morphology and EIS before and after cycling, we proposed a schematic diagram, as shown in **Figure7F**, to explain the lithium storage mechanism. In the SnO_2–TiO_2 composite thin-film electrodes, there is no conversion reaction or alloying reaction between TiO_2 and lithium. The $(Li_x)TiO_2$ may act as a stable membrane during charge-discharge processes regardless of the drastic volume change of Li_xSn, possibly causing the enhanced cyclability. For the SnO_2–Fe_2O_3 thin-film electrode, the addition of an extra conversion component Fe_2O_3, not only provides new Li^+ hosts but also increases the conductivity of the electrode by introducing metallic Fe from the conversion reaction between lithium and Fe_2O_3 after full discharge. For the SnO_2–ZnO composite thin-film electrode, the improved performance can be attributed to the combined advantages of large capacity of SnO_2 and ZnO. The obvious synergistic effect between ZnO and SnO_2 is that during discharging process, SnO_2 reacts with Li at a higher potential (~0.76 V) than ZnO (~0.61 V), forming metallic Sn nanograins surrounding ZnO particles before they get lithiated, which may help to suppress the ZnO volume expansion and in return preventing the Sn nanograins from aggregation in the following lithiation of ZnO. In this way, the capacity fading of SnO_2–ZnO composite can be relieved and cycling life can be extended.

CONCLUSIONS

We have exploited the benefits of ALD to fabricate uniform, smooth and well atomically intermixed SnO_2–TiO_2, SnO_2–Fe_2O_3 and SnO_2–ZnO composite thin-film model electrodes to evaluate their electrochemical performance as anode materials for LIBs. Cycling stability discloses the effect of synergy on battery capacity performance. All the composite thin-films (SnO_2–TiO_2, SnO_2–Fe_2O_3 and SnO_2–ZnO) show better electrochemical properties, either higher capacity, better retention or improved rate capability as compared to the individual components (SnO_2, TiO_2, Fe_2O_3 and ZnO). With the addition of TiO_2, the composite

thin-films achieve lower overall capacity but obtain excellent cyclability. With incorporation of Fe_2O_3 in the composite thin-films, both the capacity and retention are improved, but both have moderate effect. With regards to the addition of ZnO, the composite thin-films can be stabilized at higher capacity than the bare components after a capacity drop in the few initial cycles. The SnO_2–ZnO composite thin-film electrodes eventually obtain the best comprehensive performance amongst the tested materials. This work reports a systematic study of the synergistic effects between two different types of metal oxide and can hopefully provide a useful guidance for the development of better composite anode materials for thin-film rechargeable batteries.

DATA AVAILABILITY STATEMENT

The original contributions presented in the study are included in the article/Supplementary Material, further inquiries can be directed to the corresponding author.

AUTHOR CONTRIBUTIONS

CD conceived the original idea and supervised the writing. BZ did all the experiments and data analysis, plotted the figures, wrote the original draft. AD and JD revised the manuscript.

FUNDING

The authors acknowledge FWO-Vlaanderen (Nos. GO87418N and 1S68518N), and BOF-UGent (Nos. 01G01513 and 01G01019) for financial support.

ACKNOWLEDGMENTS

The authors also acknowledge Dr. Matthias Minjauw for assistance with the XPS measurements and analysis, and thank Olivier Janssens for SEM measurements.

REFERENCES

Ban, C. M., Xie, M., Sun, X., Travis, J. J., Wang, G. K., Sun, H. T., et al. (2013). Atomic layer deposition of amorphous TiO_2 on graphene as an anode for Li-ion batteries. *Nanotechnology* 24 (42), 424002. doi:10.1088/0957-4484/24/42/424002

Bruck, A. M., Cama, C. A., Gannett, C. N., Marschilok, A. C., Takeuchi, E. S., and Takeuchi, K. J. (2016). Nanocrystalline iron oxide based electroactive materials in lithium ion batteries: the critical role of crystallite size, morphology, and electrode heterostructure on battery relevant electrochemistry. *Inorg. Chem. Front.* 3 (1), 26–40. doi:10.1039/c5qi00247h

Chen, J. S., and Lou, X. W. (2013). SnO_2-based nanomaterials: synthesis and application in lithium-ion batteries. *Small* 9 (11), 1877–1893. doi:10.1002/smll.201202601

Chen, D., Lou, Z., Jiang, K., and Shen, G. Z. (2018a). Device configurations and future prospects of flexible/stretchable lithium-ion batteries. *Adv. Funct. Mater.* 28 (51), 1805596. doi:10.1002/adfm.201805596

Chen, X. F., Huang, Y., Zhang, K. C., Feng, X. S., and Wang, M. Y. (2018b). Porous TiO_2 nanobelts coated with mixed transition-metal oxides Sn_3O_4 nanosheets core-shell composites as high-performance anode materials of lithium ion batteries. *Electrochim. Acta* 259, 131–142. doi:10.1016/j.electacta.2017.10.180

Cheong, J. Y., Kim, C., Jung, J. W., Yoon, K. R., and Kim, I. D. (2018). Porous SnO_2-CuO nanotubes for highly reversible lithium storage. *J. Power Sources* 373, 11–19. doi:10.1016/j.jpowsour.2017.10.090

Dendooven, J., Deduytsche, D., Musschoot, J., Vanmeirhaeghe, R. L., and Detavernier, C. (2010). Conformality of Al_2O_3 and AlN deposited by plasma-enhanced atomic layer deposition. *J. Electrochem. Soc.* 157 (4), G111–G116. doi:10.1149/1.3301664

Deng, S., Kurttepeli, M., Cott, D. J., Bals, S., and Detavernier, C. (2015). Porous nanostructured metal oxides synthesized through atomic layer deposition on a carbonaceous template followed by calcination. *J. Mater. Chem. A* 3 (6), 2642–2649. doi:10.1039/C4TA05165C

Dobbelaere, T., Vereecken, P. M., and Detavernier, C. (2017). A USB-controlled potentiostat/galvanostat for thin-film battery characterization. *HardwareX* 2, 34–49. doi:10.1016/j.ohx.2017.08.001

Fang, R. P., Chen, K., Yin, L. C., Sun, Z. H., Li, F., and Cheng, H. M. (2019). The regulating role of carbon nanotubes and graphene in lithium-ion and lithium-sulfur batteries. *Adv. Mater.* 31 (9), 1800863. doi:10.1002/adma.201800863

Fang, S., Bresser, D., and Passerini, S. (2020). Transition metal oxide anodes for electrochemical energy storage in lithium-and sodium-ion batteries. *Adv. Energy Mater.* 10 (1), 1902485. doi:10.1002/aenm.201902485

Ferraresi, G., Villevieille, C., Czekaj, I., Horisberger, M., Novak, P., and El Kazzi, M. (2018). SnO_2 model electrode cycled in Li-ion battery reveals the formation of Li_2SnO_3 and Li_8SnO_6 phases through conversion reactions. *ACS Appl. Mater. Interfaces* 10 (10), 8712–8720. doi:10.1021/acsami.7b19481

Gu, Y., Jiao, Z., Wu, M. H., Luo, B., Lei, Y., Wang, Y., et al. (2017). Construction of point-line-plane (0-1-2 dimensional) Fe_2O_3-SnO_2/graphene hybrids as the anodes with excellent lithium storage capability. *Nano Res.* 10 (1), 121–133. doi:10.1007/s12274-016-1271-y

Ha, D. H., Islam, M. A., and Robinson, R. D. (2012). Binder-free and carbon-free nanoparticle batteries: a method for nanoparticle electrodes without polymeric binders or carbon black. *Nano Lett.* 12 (10), 5122–5130. doi:10.1021/nl3019559

He, M., Yuan, L. X., Hu, X. L., Zhang, W. X., Shu, J., and Huang, Y. H. (2013). A SnO_2@carbon nanocluster anode material with superior cyclability and rate capability for lithium-ion batteries. *Nanoscale* 5 (8), 3298–3305. doi:10.1039/c3nr34133j

Jahel, A., Ghimbeu, C. M., Monconduit, L., and Vix-Guterl, C. (2014). Confined ultrasmall SnO_2 particles in micro/mesoporous carbon as an extremely long cycle-life anode material for Li-ion batteries. *Adv. Energy Mater.* 4 (11), 1400025. doi:10.1002/aenm.201400025

Kim, D. W., Hwang, I. S., Kwon, S. J., Kang, H. Y., Park, K. S., Choi, Y. J., et al. (2007). Highly conductive coaxial SnO_2-In_2O_3 heterostructured nanowires for li ion battery electrodes. *Nano Lett.* 7 (10), 3041–3045. doi:10.1021/nl0715037

Kim, H., Park, G. O., Kim, Y., Muhammad, S., Yoo, J., Balasubramanian, M., et al. (2014). New insight into the reaction mechanism for exceptional capacity of ordered mesoporous SnO_2 electrodes via synchrotron-based X-ray analysis. *Chem. Mater.* 26 (22), 6361–6370. doi:10.1021/cm5025603

Kim, T., Song, W. T., Son, D. Y., Ono, L. K., and Qi, Y. B. (2019). Lithium-ion batteries: outlook on present, future, and hybridized technologies. *J. Mater. Chem. A* 7 (7), 2942–2964. doi:10.1039/c8ta10513h

Kint, J., Mattelaer, F., Minjauw, M., Zhao, B., and Detavernier, C. (2019). Atomic layer deposition of thin films as model electrodes: a case study of the synergistic effect in Fe_2O_3-SnO_2. *J. Vac. Sci. Technol. A* 37 (5), 050904. doi:10.1116/1.5115987

Li, Q., Li, H., Xia, Q., Hu, Z., Zhu, Y., Yan, S., et al. (2020). Extra storage capacity in transition metal oxide lithium-ion batteries revealed by *in situ* magnetometry. *Nat. Mater.* doi:10.1038/s41563-020-0756-y

Li, S., Ling, M., Qiu, J. X., Han, J. S., and Zhang, S. Q. (2015a). Anchoring ultra-fine TiO_2-SnO_2 solid solution particles onto graphene by one-pot ball-milling for long-life lithium-ion batteries. *J. Mater. Chem. A* 3 (18), 9700–9706. doi:10.1039/c5ta01350j

Li, Y., Yu, S. L., Yuan, T. Z., Yan, M., and Jiang, Y. Z. (2015b). Rational design of metal oxide nanocomposite anodes for advanced lithium ion batteries. *J. Power Sources* 282, 1–8. doi:10.1016/j.jpowsour.2015.02.016

Liu, D. Q., Liu, Z. J., Li, X. W., Xie, W. H., Wang, Q., Liu, Q. M., et al. (2017). Group IVA element (Si, Ge, Sn)-Based alloying/dealloying anodes as negative electrodes for full-cell lithium-ion batteries. *Small* 13 (45), 1702000. doi:10.1002/smll.201702000

Lu, S. T., Wang, H. H., Zhou, J., Wu, X. H., and Qin, W. (2017). Atomic layer deposition of ZnO on carbon black as nanostructured anode materials for high-performance lithium-ion batteries. *Nanoscale* 9 (3), 1184–1192. doi:10.1039/c6nr07868k

Lu, Y., Yu, Y., and Lou, X. W. (2018). Nanostructured conversion-type anode materials for advanced lithium-ion batteries. *Chem* 4 (5), 972–996. doi:10.1016/j.chempr.2018.01.003

Mattelaer, F., Vereecken, P. M., Dendooven, J., and Detavernier, C. (2015). Deposition of MnO anode and MnO_2 cathode thin films by plasma enhanced atomic layer deposition using the $Mn(thd)_3$ precursor. *Chem. Mater.* 27 (10), 3628–3635. doi:10.1021/acs.chemmater.5b00255

Musschoot, J., Xie, Q., Deduytsche, D., Van den Berghe, S., Van Meirhaeghe, R. L., and Detavernier, C. (2009). Atomic layer deposition of titanium nitride from TDMAT precursor. *Microelectron. Eng.* 86 (1), 72–77. doi:10.1016/j.mee.2008.09.036

Pender, J. P., Jha, G., Youn, D. H., Ziegler, J. M., Andoni, I., Choi, E. J., et al. (2020). Electrode degradation in lithium-ion batteries. *ACS Nano* 14 (2), 1243–1295. doi:10.1021/acsnano.9b04365

Qi, W., Shapter, J. G., Wu, Q., Yin, T., Gao, G., and Cui, D. X. (2017). Nanostructured anode materials for lithium-ion batteries: principle, recent progress and future perspectives. *J. Mater. Chem. A* 5 (37), 19521–19540. doi:10.1039/c7ta05283a

Ramachandran, R. K., Dendooven, J., and Detavernier, C. (2014). Plasma enhanced atomic layer deposition of Fe_2O_3 thin films. *J. Mater. Chem. A* 2 (27), 10662–10667. doi:10.1039/c4ta01486c

Reddy, M. V., Rao, G. V. S., and Chowdari, B. V. R. (2013). Metal oxides and oxysalts as anode materials for Li ion batteries. *Chem. Rev.* 113 (7), 5364–5457. doi:10.1021/cr3001884

Roselin, L. S., Juang, R. S., Hsieh, C. T., Sagadevan, S., Umar, A., Selvin, R., et al. (2019). Recent advances and perspectives of carbon-based nanostructures as anode materials for Li-ion batteries. *Materials* 12 (8), 1229. doi:10.3390/ma12081229

Su, X., Wu, Q. L., Li, J. C., Xiao, X. C., Lott, A., Lu, W. Q., et al. (2014). Silicon-based nanomaterials for lithium-ion batteries: a review. *Adv. Energy Mater.* 4 (1), 1300882. doi:10.1002/aenm.201300882

Wadewitz, D., Gruner, W., Herklotz, M., Klose, M., Giebeler, L., Voss, A., et al. (2013). Investigation of copper-cobalt-oxides as model systems for composite interactions in conversion-type electrodes for lithium-ion batteries. *J. Electrochem. Soc.* 160 (8), A1333–A1339. doi:10.1149/2.014309jes

Wang, Y. Z., Han, J. S., Gu, X. X., Dimitrijev, S., Hou, Y. L., and Zhang, S. Q. (2017). Ultrathin Fe_2O_3 nanoflakes using smart chemical stripping for high performance lithium storage. *J. Mater. Chem. A* 5 (35), 18737–18743. doi:10.1039/c7ta05798a

Wei, W., Wang, Z., Liu, Z., Liu, Y., He, L., Chen, D., et al. (2013). Metal oxide hollow nanostructures: fabrication and Li storage performance. *J. Power Sources* 238, 376–387. doi:10.1016/j.jpowsour.2013.03.173

Wen, Z. H., Wang, Q., Zhang, Q., and Li, J. H. (2007). *In situ* growth of mesoporous SnO_2 on multiwalled carbon nanotubes: a novel composite with porous-tube structure as anode for lithium batteries. *Adv. Funct. Mater.* 17 (15), 2772–2778. doi:10.1002/adfm.200600739

Wu, F. F., Bai, J., Feng, J. K., and Xiong, S. L. (2015). Porous mixed metal oxides: design, formation mechanism, and application in lithium-ion batteries. *Nanoscale* 7 (41), 17211–17230. doi:10.1039/c5nr04791a

Xie, M., Sun, X., George, S. M., Zhou, C. G., Lian, J., and Zhou, Y. (2015). Amorphous ultrathin SnO_2 films by atomic layer deposition on graphene network as highly stable anodes for lithium-ion batteries. *ACS Appl. Mater. Interfaces* 7 (50), 27735–27742. doi:10.1021/acsami.5b08719

Xie, Q., Jiang, Y. L., Detavernier, C., Deduytsche, D., Van Meirhaeghe, R. L., Ru, G. P., et al. (2007). Atomic layer deposition of TiO_2 from tetrakis-dimethyl-amido titanium or Ti isopropoxide precursors and H_2O. *J. Appl. Phys.* 102 (8), 083521. doi:10.1063/1.2798384

Yan, X. D., Wang, Z. H., He, M., Hou, Z. H., Xia, T., Liu, G., et al. (2015). TiO_2 nanomaterials as anode materials for lithium-ion rechargeable batteries. *Energy Technol.* 3 (8), 801–814. doi:10.1002/ente.201500039

Yi, Z., Han, Q. G., Zan, P., Cheng, Y., Wu, Y. M., and Wang, L. M. (2016). Facile fabrication of SnO_2@TiO_2 core-shell structures as anode materials for lithium-ion batteries. *J. Mater. Chem. A* 4 (33), 12850–12857. doi:10.1039/c6ta03915d

Yuan, T., Tan, Z. P., Ma, C. R., Yang, J. H., Ma, Z. F., and Zheng, S. Y. (2017). Challenges of spinel $Li_4Ti_5O_{12}$ for lithium-ion battery industrial applications. *Adv. Energy Mater.* 7 (12), 1601625. doi:10.1002/aenm.201601625

Zhang, W. J. (2011). Lithium insertion/extraction mechanism in alloy anodes for lithium-ion batteries. *J. Power Sources* 196 (3), 877–885. doi:10.1016/j.jpowsour.2010.08.114

Zhao, B., Huang, S. Y., Wang, T., Zhang, K., Yuen, M. M. F., Xu, J. B., et al. (2015a). Hollow SnO_2@Co_3O_4 core-shell spheres encapsulated in three-dimensional graphene foams for high performance supercapacitors and lithium-ion batteries. *J. Power Sources* 298, 83–91. doi:10.1016/j.jpowsour.2015.08.043

Zhao, Q. Q., Ma, L. S., Zhang, Q., Wang, C. G., and Xu, X. J. (2015b). SnO_2-based nanomaterials: synthesis and application in lithium-ion batteries and supercapacitors. *J. Nanomater.* 2015, 850147. doi:10.1155/2015/850147

Zhao, Y., Li, X. F., Yan, B., Xiong, D. B., Li, D. J., Lawes, S., et al. (2016). Recent developments and understanding of novel mixed transition-metal oxides as anodes in lithium ion batteries. *Adv. Energy Mater.* 6 (8), 1502175. doi:10.1002/aenm.201502175

Zhao, B., Mattelaer, F., Kint, J., Werbrouck, A., Henderick, L., Minjauw, M., et al. (2019). Atomic layer deposition of ZnO–SnO_2 composite thin film: the influence of structure, composition and crystallinity on lithium-ion battery performance. *Electrochim. Acta* 320, 134604. doi:10.1016/j.electacta.2019.134604

Zheng, M. B., Tang, H., Li, L. L., Hu, Q., Zhang, L., Xue, H. G., et al. (2018). Hierarchically nanostructured transition metal oxides for lithium-ion batteries. *Adv. Sci.* 5 (3), 1700592. doi:10.1002/advs.201700592

Zhu, G. N., Wang, Y. G., and Xia, Y. Y. (2012). Ti-based compounds as anode materials for Li-ion batteries. *Energy Environ. Sci.* 5 (5), 6652–6667. doi:10.1039/c2ee03410g

Zoller, F., Bohm, D., Bein, T., and Fattakhova Rohlfing, D. (2019). Tin oxide based nanomaterials and their application as anodes in lithium-ion batteries and beyond. *Chemsuschem* 12 (18), 4140–4159. doi:10.1002/cssc.201901487

Conflict of Interest: The authors declare that the research was conducted in the absence of any commercial or financial relationships that could be construed as a potential conflict of interest.